UCRL-ID-139812

Hot Electron Diagnostic in a Solid Laser Target by K-Shell Lines Measurement from Ultra-Intense Laser-Plasma Interactions (λ = 1.06 μm, 3x10^{20} W cm^{-2}, $\leq$ 500 J)

K. Yasuike, K.B. Wharton, M.H. Key, S.P. Hatchett, R.A. Snavely

July 27, 2000

U.S. Department of Energy
Lawrence Livermore National Laboratory

DISCLAIMER

This work was performed under the auspices of the U. S. Department of Energy by the University of California, Lawrence Livermore National Laboratory under Contract No. W-7405-Eng-48.

Hot electron diagnostic in a solid laser target by K-shell lines measurement from ultra-intense laser-plasma interactions (λ = 1.06 μm, $3x10^{20}$ W cm^{-2}, ≤ 500 J)

K. Yasuike, K.B. Wharton, M.H. Key, S.P. Hatchett, R.A. Snavely

Abstract

Characterization of hot electron production (a conversion efficiency from laser energy into electrons) from ultra intense laser-solid target interaction by observing molybdenum (Mo) Kβ as well as Kα emissions from a buried fluorescence tracer layer in the targets has been done. The experiments used 1.06 μm laser light with an intensity of from $2x10^{18}$ up to $3x10^{20}$ W cm^{-2} (20 – 0.5 ps pulse width) and an on target laser energy of 280-500 J. The conversion efficiency from the laser energy into the energy, carried by hot electrons, has been estimated to be ~50 % for the 0.5 ps shots at an on-target laser intensity of $3x10^{20}$ W cm^{-2}, which increased from ~30 % at $1x10^{19}$ W cm^{-2} 5 ps shots and ~12 % at $2x10^{18}$ W cm^{-2} 20 ps shots.

1 Introduction

Characterization of hot electrons generated in laser-matter interactions is an important topic, now accessible at new laser intensities thanks to recent developments in ultra-high intensity lasers, and is relevant to fast ignitor (FI) scheme for inertial confinement fusion (ICF). Resonant [1] and not-so-resonant absorption mechanisms [2] may be major factors in determining the coupling efficiency from laser to the plasma [3], in which electrons are major carriers of the input energy. The FI scheme originated by M. Tabak [1] relies on these electrons, as do recently discovered ion acceleration phenomena [2, 3,4] that could potentially replace the electrons in the original FI concept [5]. Characterization of hot electron production is crucial for

understanding the ultra-intense field physics of the high intensity laser interactions, and also is of critical importance in assessing the feasibility of both types of FI concepts. Ultra-intense laser experiments along these lines are being carried out at several laboratories [6-12].

The scaling of hot electron temperature T_H with $I\lambda^2$ (where I is laser intensity and λ is laser wavelength) is a classic question, empirically scaling as $T_H = 4x10^{-7}$ $(I\lambda^2)^{0.5}$ keV, (for I in W cm^{-2} and λ in μm) under a laser intensity of $\leq 2x10^{15}$ W cm^{-2} for 1.06, 0.53 and 0.26 μm wavelengths [Amiranoff et. al. in 1982]. Teubner et. al. [19] and Beg et al. [8] extended an empirical $T_H \propto I^{0.3}$ scaling up to 10^{19} W cm^{-2}. Experiments in the mid-10^{19} W cm^{-2} have now been carried out [5, 6, 7, 10, 18, 20].

In 1979, Hares [13] established the buried Kα fluorer layer method as an indirect way to estimate the hot electron spectrum. This technique was extended to higher intensities by Ebrahim [14] and Luther-Davis [15], the latter of which obtained a laser-hot electron conversion efficiency of 3%. This technique was used for short pulse (≤1.3 ps) laser experiments by Chen [16], by Rousse [17] who observed that ~70 % of incident laser was absorbed, and by Jiang [18] with a 300 fs laser up to 10^{19} W cm^{-2}. In recent experiments done by Hall [7] to investigate hot electron propagation within a shock compressed matter, and experiments by Schlegel [21] and Bastiani

[22] to study effects of plasma scale length, the technique became an indispensable diagnostic. The buried layer method is especially relevant to the electron FI scheme as the electrons are measured before they leave the target. By varying the front layer thickness, the number of hot electrons which reach the tracer layer can be modified, and therefore the K-shell x-ray emissions excited by the hot electrons are a function of this front layer thickness. Comparing the experimental variation of K-shell emissions obtained experimentally to a monte-carlo model enables the characterization of hot electron temperature and laser-to-electron conversion efficiency.

This paper reports the results of K-shell (Kα and Kβ) emission measurements from a buried layer on Petawatt laser shots [23] at LLNL. In our experiments, the laser energy was typically 400 J, and the laser power was varied from 20 TW up to ~1 PW (10^{18} up to $3x10^{20}$ W cm^{-2}) by decreasing the pulse duration of the laser from 20 ps to 0.5 ps. The expected electron energy from these laser-solid interactions can be roughly estimated from the empirical $I\lambda^2$ values discussed above. The hot electron energy spectrum could be considered to be in same order of ponderomotive potential [24] theoretically determined by the $I\lambda^2$ as $U_{pond} \cong \{\sqrt{(1+ I\lambda^2 / 2.8)} - 1\}$ x 511 [keV], where I and λ in 10^{18} W cm^{-2} and μm, respectively. The U_{pond} comes to be ≤ 5.9 MeV (≤ 470 keV) for a laser intensity of $3x10^{20}$ W cm^{-2} ($1x10^{18}$). More realistically, from

the empirical expression $E \propto I^{0.3}$ (where E is electron energy), $E \leq$ 760 keV at 10^{18} W cm^{-2} [8] and would be $E \leq 1.4$ MeV at $3x10^{20}$ W cm^{-2} if this relationship remains valid. The results presented in this paper are the first measurements which test the applicability of this scaling to the 10^{20} W cm^{-2} intensity regime of laser-solid interactions.

2. Experimental design

2.1 Target structure

The structure of the target is shown in the inset 1 in the fig 1, and is the same used in conducted experiments [10] at the 100TW laser system at LLNL. The target is built of three layers, aluminum (Al), molybdenum (Mo) and plastic (CH). The first or front layer, is the incident layer for the laser-plasma interaction. The variable fraction of forward driven electrons as well as x-rays from the incident Al layer, penetrate into the 50μm thickness of fluorescent Mo tracer layer. Both of these processes excite the K-shell characteristic x-rays that are observed. We varied the front layer thickness from 0.05 g cm^{-2} up to 0.27 g cm^{-2} (200 μm to 1000 μm thickness.) to attenuate the electron flux. These K-shell x-rays are observed by a CCD spectrometer, where we may infer the electron flux incident on the tracer layer.

The spectrometer is a charge-coupled device (CCD) operated in a single photon mode, in which each pixel detects one photon or less. The read-out count

values for the pixels are proportional to the photon energies. The CCD covers a relatively large solid angle and has sufficient energy resolution for these experiments. There are significant amounts of tin (Sn) and lead (Pb) inside the CCD camera in the form of solder. It has a very large solid angle against the CCD than x-rays from the target. The Mo tracer layer is chosen for its characteristic emission lines, Kα2 17.374 keV (with K-shell intensity ratio of 22.4 %,) Kα1 17.479 keV (42.7 %,) Kβ3 19.590 keV (3.42 %,) Kβ1 19.607 keV (6.63 %,) Kβ2 19.965 keV (1.45 %) and Kβ4 19.998 keV (0.302 %) in energy ascending order, which uniquely distinguish themselves from the background elemental line emissions, e.g., Pb $L_{\beta}2$ and 1 (in stronger order, 12.6 keV,) Pb $L_{\beta}5$ (13.015 keV,) Pb $L_{\gamma}1$ (14.765 keV,) Sn Kα2 and 1 (25.19 keV,) Sn Kβ3 and 1 (28.47 keV) and Sn Kβ2 and 4 (29.12 keV) present in the spectrometer. Additionally the tracer lines should be high enough in energy to avoid photo excitation by a strong bremsstrahlung x-ray background but not so very high that photon acquisition efficiency of the CCD is reduced and its energy resolution will be deteriorated by Compton effects [25]. The Mo Kα -(Kβ) group intensity assignments is 65.1 (11.8) respectively, with a Kβ/Kα intensity ratio of 0.18123 [26]. The thickness of the tracer layer was chosen to maximize Kα photon yields and improve the signal-to-noise (s/n) ratio in the experiments. The photon cross-section and the

radiation length of Mo for Kα (Kβ) is, respectively, $2.8x10^3$ barn and 53 μm ($2.2x10^3$ barns and 72 μm) [25]. The last (backside) layer of 1000 μm thickness CH is a protective layer which avoids the reflexing into the tracer layer of escaped electrons attracted by the target potential. (fig. 1, in-set 2). This protective layer decreases background noise and false Mo K-shell signal by the reflex electrons by more than a factor of 2 [10] and improves the s/n ratio. The cut-off energy of the protective layer for electrons is 570 keV for a double pass through the tracer layer as shown (1) in the inset figure 2 of the fig. 1) and 350 keV for a single pass ((2) in the inset.). The protective layer is used for all experiments.

2.2 Monte-Carlo K-shell x-ray yield modeling

We have Monte-Carlo modeled (Integrated Tiger Series 3.0) [27] the K-shell x-ray yield from a series of energetic monochromatic electrons incident on target and obtained the individual x-ray responses. We may combine relative intensities of each electron energy into an effective electron temperature spanning the spectrum and these, together with their responses are called the "universal curves". These universal curves provide a parameter space to estimate electron temperature and conversion efficiency for different model electron spectrum shapes. We use the experimentally observable absolute K-shell x-ray (Kα-Kβ) yields, to estimate conversion efficiency from laser energy into the energy carried by hot electrons and the temperature of the

hot electrons. The modeled yields gives limits of 100 % assuming that all the laser energy are converted into hot electrons with a specific energy distribution.

The ITS modeling showed that the inner shell of Mo can be ionized by hot electron impact and that x-ray photoionization cannot be ignored for the relatively low energy x-ray region. For Mo, the K-shell cross-section for x-rays energies from 20 keV to ~100 keV is from 10^4 to 100 barns whereas the electron ionization cross-section is nearly flat at 80 to 200 barns for electrons above 50 keV. Where a cut off energy is given as the minimum electron energy required to ionize a buried Mo atom. For electrons having half the cut-off energy for front layer penetration, evidence of the Kα x-rays was 30–45 % of those electrons of energy $E_{cut\text{-}off}$ reducing to ~5% for electrons of energy 1.5 $E_{cut\text{-}off}$. For lower electron temperatures photoionization contribution to the Kα yield is significant. The cut-off energy as a function of the Al front layer for 200, 400, 800, and 1000 μm thickness is, respectively, 195, 300, 470, and 570 keV. Though our modeling correctly accounts for the complete photon-electron cascade, the model does not account for the effects of collective motion of electrons, i.e., electric current conveyed by electrons, nor ion contributions which are discussed further in the sec. 6. It still gives reasonable estimations and good agreement with experimental results from previous experimental work [10].

Since the real electron energies are always distributed rather than being monochromatic, we obtained the universal curves as a function of temperature and not as a function of electron energy. The results of the Monte-Carlo modeling were then used to calculate the yields represented by a temperature. To illustrate the effect on Kα yield due to electron distribution shape, we choose three mono-temperature energy distributions to see variations in yield; Boltzmann: $f(E) = e^{-E/T} / T$, Maxwellian: $f(E) = 2 E^{1/2} e^{-E/T} / \pi^{1/2} T^{3/2}$, and the extreme relativistic Maxwellian: $f(E) = E^2 e^{-E/T} / 2T^3$. Where the variables E, T, f(E) are respectively, electron energy, representative temperature of the distributions and number distribution of electron as a function of energy E. Thus Kα yields as a function of representative temperature from unit hot electron energy are then obtained. Figure 2 (lower graph, using the left and bottom axis) is the resultant set of universal curves for the target structures used in these experiments (front Al layer: 200, 400, 800 and 1000 μm) for the three temperature distributions. In lower energy region (≤ 500 keV,) relativistic Maxwellian conditions give highest Kα production among these distributions since only the higher portion of the spectrum contributes to the yield. Unit total energy carried by electrons in the respective distributions, but the total numbers of the electrons in each distribution, $\int f(E)\, dE$, may be different. We confirmed that these three distribution give the same

results if we describe those temperatures by a mean energy $\overline{E}$, corresponding to kT, 1.5 kT, and 3 kT respectively for Boltzmann, Maxwellian, and relativistic Maxwellian distributions [10]. The upper graph of the fig. 2 shows the deviations of the Boltzmann and the relativistic Maxwellian from the Maxwellian curves (right axis) at the same $\overline{E}$ (upper axis). The deviations of the yield, $(Y_i - Y_{mx}) / Y_i$, where the index i represents for Boltzmann or relativistic Maxwellian case and Mx for Maxwellian, are calculated. The curve in blue (red) shows average of the ratio among the entire front layer thickness range at an $\overline{E}$ for Boltzmann (relativistic Maxwellian) and lower and upper error (or deviation) bars shows the minimum and maximum in that thickness range, so any front thickness condition falls within the envelope between the deviation bars. The relativistic Maxwellian curves register larger deviations, ≤ 85 %, in lower not relativistic energy regime. Above 700 keV, the difference among the distributions is less than 10 % and will converge to the Maxwellian curves in the higher energy region.

It is apparent from the universal curve that for higher electron temperatures, K-shell x-ray production efficiency is not very sensitive to hot electron temperature or shape of temperature distribution. However we can still estimate a conversion efficiency from K-shell photon yield, though it is difficult to say about temperature (electron spectrum.) This is plausible from the electron cut-off energies for these

specific front layer thicknesses. We should note that if there are high energy hot electron components far above the cut-off ranges, or a distorted temperature distributions from a conventional exponential mono-temperature distribution, the buried layer method would give some errors in the estimated temperature since the contribution from these components will be seen like constant floor because energy deposition within the tracer layer is near constant. However conversion efficiency can be still expected to be inferred from K-shell emission measurements.

3. Experimental set-up

We have done three experimental series with different laser pulse duration, 20 ps, 5 ps, and 0.5 ps shots, to accomplish several different laser power and intensity level to investigate these effects. The on target laser energy was from 280 up to 500 J. There were laser intensity profile structures at the laser focal spot, and shape of the profile and structures were different in each experimental series. Details of the laser intensity profile and the structures are discussed in ref. 23 . For the longer laser pulse shots at 20 ps and 5 ps, no deformable mirror was used. The laser intensity was ~$2x10^{18}$ W cm^{-2} at 20 TW laser power for 20 ps shots, and ~$1x10^{19}$ W cm^{-2} at 60 TW for 5 ps shots. For 0.5 ps shots power at 0.7–1 PW, the laser focus was improved with the addition of a deformable mirror which delivered a laser intensity of $\leq 3x10^{20}$ W cm^{-2}. The incident laser angle was 45°, at P-polarization for 5 ps and 20 ps shots and

normal incidence for the 0.5 ps shots. Previously, lower intensity shots with different incident angles of 25° and 45° were performed [10] and their results were essentially identical. Due to the amount of pre-pulse we have a significant pre-formed plasma in front of the target when the main laser pulse arrives. Thus for our laser system the effects of incident angle was not expected to significantly change laser energy absorption.

Figure 1 shows experimental set-up. An ultra-intense laser light with a beam diameter of 67 cm focused by an on-axis f/3 parabolic mirror and irradiates the target. The K-shell x-rays from the tracer layer are observed by the CCD x-ray spectrometer located in backside (opposite to the laser irradiation side) of the target with an observation angle of 30 ° to the target normal axis. In 0.5 ps shots, there is a significant gamma-ray flash from the target and from the target chamber wall surrounding it, such that more CCD filtering is needed compared to the longer pulse experiments. We choose filter thickness so that the single photon mode of operation is assured to obtain good pixel (photon) number of the fluorer line detection. In a single photon mode, soft x-rays far below the target lines at the CCD also need to be attenuated since these photons consume usable pixels which otherwise can be used for the fluorer lines. There are three major sources of the background (noise)x-rays: 1) x-rays directly from the target, 2) bremsstrahlung x-rays produced from the electrons

escaped from the target, and 3) photon (bremsstrahlung) pumped fluorescence x-rays. Environmental materials, particularly those of the CCD chip and surrounding housing, generate low energy photons from fluorescence x-rays. The distance from the target to the CCD was 4720 mm (3000 mm) for 0.5 ps (5 and 20 ps) shots. Between the target and the CCD, there was an Al vacuum - atmosphere barrier of 0.8 mm thickness located on the target chamber about 1 m from the target and was a part of the CCD filtering. Additional Al filters are placed close to the barrier so that the filters have less solid angle emission into the CCD from the fluorescence from them. The total thickness of the filter was from 5.2 to 7.6 mm (1.5 – 2.5 mm) of Al for 0.5 ps (5 and 20 ps) shots. Filter thickness was varied depending on anticipated required x-ray attenuation to keep the CCD in single photon mode.

3.1 CCD x-ray spectrometer/ Energy resolution

A charged coupled device (CCD) camera, XTEA/CCD-1024 [28] from Scientific Imaging Technologies (SITe)/Tektronix is used as the x-ray spectrometer. The CCD is placed in a housing, which has a polycarbonate window as an X-ray entrance. The attenuation by the window for Mo K-shell x-rays is negligible. The CCD has 1024 by 1024 (1 mega) pixels each with an active area of 24x24 μm^2 and a depletion layer thickness of 7 μm [28]. The temperature of the CCD chip was maintained to be –24 °C to –30 °C. Total number of pixels in the CCD determines the

accuracy of the data. The CCD registers a different eV per count and a energy resolution for hard x-ray energies than for lower energy photons, i.e., visibles and UVs [29]. The energy resolution of the CCD is experimentally measured and forms the basis for the binning analysis for the experimental results (sec. 3.3). We used a ^{109}Cd radioactive source (29 μCi) for the CCD calibration, which emits ^{109m}Ag 22 keV γ-rays. An eV/count value and a photon acquisition efficiency for the ^{109m}Ag line were first obtained, and then the efficiencies for the relevant experimental lines are derived [21, 25]. The eV/count value was determined to be 22.2 eV/count. The absolute CCD efficiencies for Mo Kα and Kβ were found to be respectively, 9.37 % and 6.54 % per incident photons hitting the CCD.

In the calibration using the radioactive source, the ^{109m}Ag line widths appearing in the CCD spectra were ~1 keV, which is significantly wider than the actual line width and also wider than the line widths observed in the data shots. This line broadning in the calibration is attributed to the longer accumulation time in the calibration, typically 60 s to 300 s, than that in the data shots of 10 ms. In order to assess the energy resolution in the real data shot condition, effects of accumulation time to the energy resolution were evaluated. Both the eV/count value and the effects of dark (background) subtraction determine the energy resolution of the CCD. Typical dark

level counts of the CCD were from 400 up to 900 counts. This dark level is comparable to the level of the counts of the signals from the relevant lines, therefore dark subtraction is necessary (indispensable) for data analysis. During the experimental series, dark images were taken before and after each data shot at the same temperature condition to subtract the dark from the data image. In order to determine the effects of dark subtraction on the energy resolution, we performed tests to take dark images before and after the data shot to evaluate the reminder (residual) counts after dark subtraction. The distributions of the histograms of residual were very close to Gaussian and depend on accumulation time and the temperatures of the CCD. We determined the full width at the half maximum (FWHM) of the distribution by Gaussian fits and obtained behavior of FWHM as a function of accumulation time. We confirmed that the FWHM is almost a constant of less than 9 counts for an accumulation time of less than one second and is broadened to ~50 counts at 300 s accumulation. The overall energy resolution of the CCD in the data shots (calibration using the radioactive source) is considered to be the eV/count value times the FWHM, or ~200 eV (~1 keV), which are consistent with the observed line widths in the CCD spectra. Using the minimum bin width to cover each Kα or Kβ line group bin width, maximizes s/n ratio since the Kα-Kβ signals obtained in the 0.5 ps experiments are at

a low level. The responses of the spectrometer including the filters for Mo Kα and Kβ lines were absolutely calibrated.

3.2 Ratio of Kα and Kβ

Using Kβ signals is useful in noisy environments, i.e., the 0.5 ps shots, which are dominated by both low energy x-rays and gamma flashes, which potentially pump higher x-ray lines. In the 0.5 ps experiments using thicker filters, the Kβ/Kα ratio at the CCD was found to be 1.5 to 4 from the original Kβ/Kα ratio of ~0.18. Thicker filtering to reduce to noise level also modifies the transmitted spectra attenuating Kα lines more than the Kβ lines. In these shots we are able to perform the same analysis on Kβ lines as Kα lines.

3.3 Simulations of binning analysis for the 0.5 ps experiments

In real 0.5 ps experiments, the s/n ratio decreased and at the same time, absolute signal level (numbers of the pixels of the K-shell lines) also decreased due to the thicker filtering used with regard to the longer pulse experiments. The acquired photon number decreased to around 100 pixels (photons), which is much lower than that in 5 or 20 ps experiments of 700 or up. Because the signal response for those low photon levels was not obvious, we investigated the signal response due to a different binning analysis using computationally simulated signals, and established a processing response useful at very low s/n ratios. The results from the simulation

suggest that 1) A bin width of 6 or greater for Kβ signal and a width of 10 or greater for Kα signal should be used, and 2) A sufficient linearity in the response for the number of pixels from 20 (40) to 100 for Kβ (Kα) signal was assured. The Kβ signal can be seen in smaller bin widths and the analysis gives a lower noise floor than for Kα because Kβ3 and Kβ1 contain 85 % of the total Kβ intensity and are very closely located together within 17 eV, or less than one count. Kα signal intensities are more sparsely distributed, i.e., 34.4 and 65.6 % for Kα2 and Kα1 lines with the energy separation of 105 eV, respectively, and the Kα signal processing needs larger bin width of ≥4.7 counts than for Kβ. We found that for the case of weak Kβ signals, that by restricting the bin width, to include the Kβ1 and Kβ3 lines which contain 85% of the total Kβ intensity, is more favorable for the s/n ratio than to have a wider bin width to cover whole the Kβ group. We used a bin width of 9 for the Kβ signal analysis and a width of 11 for the Kα. The further details of the analysis is described in ref. [30 (the RSI paper)].

3.4 Fluorescence excited lines by background x-rays

We have observed some lines other than Mo K-shell lines that can be seen only in the 0.5 ps laser shots but not in the Cd source calibration runs or the longer pulse experiments. These lines were stronger than the Mo K-shell lines and were determined to be fluorescence x-rays from environmental materials (CCD) and not

from the target. These experimentally observed lines were determined to be from lines excited by the intense hard background x-rays (gamma flash) by testing the CCD camera on a 4 MeV linac., We used the linac as a Petawatt 0.5 ps shot background x-ray simulator, which reproduced the environmental line signals located at the same energy even though there is no Mo target. Existence of a hard x-ray spectrum on Petawatt experiments was established by a series of experiments using heavily filtered x-ray films, PIN diodes and photo-nuclear activation [2, 9, 11]. The photon numbers other than Mo K-shell lines from the CCD well agree with the estimation, accounting for the amount of Sn contained in the solder in the CCD camera housing and the solid angle of the Sn to the CCD chip. This turned out to be beneficial since we used the Sn Kα lines as a reference to determine absolute Mo line locations because absolute line relations may shift during the dark subtraction due to a temperature drift on the CCD chip between image acquisitions.

4. Experimental results

4.1 The 20 ps and 5 ps experiments Kα results

In these longer pulse experiments, we used only the Kα lines since the noise level to the CCD spectrometer was much less. The photon number of Kα emission was greater than for the Kβ since the thin Al filtering did not modify the original Kβ/Kα

ratio as drastically as in the 0.5 ps experiments. Typical Kα photon numbers were from 10^4 to 700. The Kα yields from 20 ps and 5 ps experiments are shown in the fig. 3a (points represented by the circle symbols) and 3b (square symbols), respectively. The curves in the figures are discussed in the sec. 5.1. A bin width of 7 was used in the analysis for these 20 ps and 5 ps results.

4.2 The 0.5 ps experiments Kα and β yield results

In order to confirm that all the CCD operations were under single photon mode, we checked the pixel usage for each shot. The shape of the CCD spectra from the 0.5 ps shots were very different from the spectra on lower laser energy shots (10^{15} w cm^{-2} [16], ~10^{16} w cm^{-2} [17], 10^{18}–10^{19} w cm^{-2} [8, 18]). The spectra had a significantly large slope decreasing towards the higher energy, even though in these experiments we used thicker filters whose x-ray attenuation tapered off very sharply toward the higher photon energy and flattened the spectra. Data analysis for these shots is discussed in detail in another paper [30]. Figure 3c shows Kα and Kβ photon production yields per unit laser energy and solid angle are plotted as a function of the front layer thickness. The points in blue in the figure represent Kα production efficiencies, in the left axis, and the points in red correspond to Kβ production, in the right axis. The right axis in the figure is scaled at the Kβ / Kα intensity ratio of 0.18 to

the left axis, so that the reading at the left axis for the Kβ data directly gives Kα equivalent numbers for the Kβ plots. The lower energy Kα signals are affected by greater x-ray noise, due to the slope of the background spectra. Thus the absolute noise level (floor) around the Kα lines are higher than Kβ's, and Kα lines and the intensity distribution are more sparsely located (sec. 3.3). This means that for some shots, the Kα signal was overwhelmed by the noise floor, although Kβ counterparts for the same shots were sufficiently out of the noise floor. We have good agreement between the Kα and Kβ results. Error bars were obtained with a standard deviation (1 σ) of the binned signal peaks with different binning center locations. Details are discussed in the ref. 30. Other curves in the fig. 3a are from interpretations of these Kβ and Kα yields into the conversion efficiencies, which are discussed in the sec. 5.2.

5. Determination of hot electron temperature and its conversion efficiencies from K-shell yields – chi-square fits and the errors

5.1 The 20 ps and 5 ps experimental series

We performed two-parameter chi-square fits to estimate hot electron temperature and the conversion efficiency using the universal curves. Solid curves in the fig. 3a (3b) shows chi-square fitting results for the 20 ps (5 ps) experimental results, assuming a Boltzmann, Maxwellian and relativistic Maxwellian temperature distributions. The curves for the three temperature distributions are almost identical

with almost same conversion efficiencies though the representative temperatures differ, which is clearly seen in the fig. 3a and 3b. Figure 4 shows the chi-square behaviors (lower graph in blue) along with the conversion efficiency behaviors (upper graph in red) as a function of temperature. These are obtained from several temperature-constrained chi-square fits by changing the presumed temperature. The chi-squares for 20 ps (5 ps) shots are shown as circle (triangle) points in the figure. As clearly seen in the fig. 4, the chi-squares converge (dip) in the plots and the 20 ps experiments show good sensitivity to estimated temperatures. This ability of positive temperature determinations is consistent with an expectation of a temperature range from the empirical law and the shapes of the universal curves. The chi-square 5 ps dip became shallow with increasing temperature when compared with the 20 ps dip. Note that the conversion efficiency around these chi-square dips remains relatively unaffected with temperature though the chi-square value varies. We find the temperatures and conversion efficiencies for the Boltzmann, Maxwellian, and relativistic Maxwellian for 20 ps data set are 328 keV ($\overline{E}$ = 328 keV) and 13.9 %, 269 keV (404 keV) 12.9 %, and 174 keV (522 keV) 11.7 %, respectively, and for 5 ps data sets are, 818 keV ($\overline{E}$ = 818 keV) and 19.4 %, 620 keV (930 keV) and 20.3 %, and 353 keV (1059 keV) and 17.1 %. The mean energies in the sets are all at the same level as expected from the upper graph of the fig. 2.

We may use unweighted chi-square fits to estimate a uniform error if we assume that each point in the same data set has a uniform error. The uniform error for a data set is a square root of the number that is the chi-square from the unweighted chi-square fit divided by number of the data points. We performed this uniform weighting fit to obtain uniform errors for each data set, 0.5 ps, 5 ps and 20 ps. In the figs. 3a and b, the fine dash curves in the figures represent the results from uniform weighting fits, and the error bars in blue on the extreme right represent the uniform errors from the unweighted chi-square fits. The resultant curves from the unweighted fits are very similar from the fit results using weighting as seen in the figures (fig. 3a and 3b). Thus the resultant uniform error bars are consistent with the error bars obtained experimentally.

5.2 The 0.5 ps experimental series

Conversion efficiencies can be positively estimated from the K-shell production yields if we know the temperature of hot electrons and the shape of energy spectrum of the hot electrons as seen in longer pulse experiments. However in the 0.5 ps experiments, the electron temperature is expected to be in the regime where the sensitivity of the universal curves to temperature is small (fig. 2). Still we could roughly estimate the electron temperature in 0.5 ps shots from theory or empirical relation. Assuming the estimated electron temperatures are between 1 MeV and 4 MeV from other x-ray

measurements [2, 9, 11], we can estimate the conversion efficiency without much error, because the universal curves for the different front layer thickness and different temperature distributions converge in high temperature region. In order to confirm that the temperatures are not below these regions, we calculated chi-squares and conversion efficiencies by presuming temperature between 400 keV and 4 MeV with the same process used for the longer pulse experiments. The resultant conversion efficiencies and chi-squares as a function of the temperature are plotted in fig. 4. For 0.5 ps shots, conversion efficiencies and chi-squares are calculated separately for the both cases: a) using Kβ results only (filled square symbols in the fig. 4), and b) using both Kα and Kβ results (empty square symbols in the fig. 4). This is intended to test the differences due to the lower s/n ratio in Kα results. The sensitivity to the estimated temperature for the 0.5 ps results are almost nil for both Kβ only and Kα and Kβ set. The assumption of electron temperature for the 0.5 ps shots is bolstered by the results of the thinner front layers where there is no significant difference from of the thicker front layer results (fig. 3c). Now, if the spectrum is assumed to be multi temperature and the major lower energy components above the cut-off of thinner thickness of 800 μm exists, then this insignificant difference would not be seen. Thus we could conclude that there are no significant large low temperature components in the hot electron spectra. The chi-

squares of 0.5 ps shots including Kα results are higher than those from the fits using only Kβ results. Therefore we adopt the conversion efficiency estimation from the Kβ results. We defined the "standard" conversion efficiency for the 0.5 ps shots to be of 2 MeV mean energy, which corresponds to 3, 2 and 1 MeV temperature for Boltzmann, Maxwellian, and relativistic Maxwellian respectively. The green dotted curve (red dash-dot, blue dash-dot curves) in upper portion of fig. 3c represents the 100 % standard conversion efficiencies for Maxwellian (relativistic Maxwellian, Boltzmann), quoted from the universal curves. These curves differ slightly but the shapes are almost identical. The blue and red dotted curves in the fig. 3c represent, respectively, the 100 % conversion efficiencies for 2 MeV temperature Boltzmann, Maxwellian, and relativistic Maxwellian distribution. The "standard" efficiencies for 0.5 ps shots are determined to be 50.87±2.73 % (1σ,) 47.68±3.85 % and 44.16±3.57 % for Boltzmann, Maxwellian, and Relativistic Maxwellian distributions, respectively.

The uniform errors for Kβ only (Kα and Kβ) estimated from unweighted fits for the standard temperature are shown in blue on extreme right (left) in the fig. 3c. These uniform errors in the 0.5 ps experiments are not sensitive to the temperature as well (fig. 4).

6. Discussion

Ion contribution

There have been some reports on generating energetic ions at high-intensity laser-plasma experiments. Effects of K-shell x-rays excited by energetic ions inside the target may be estimated. Even with observed fast ions of 10^{12} protons per shot the K-shell excitation is insignificantly low [3]. The Mo K-shell excitation efficiencies by ions are from 0.3 to 80 barns for 1 to 3 MeV/a.m.u or $3.8\text{x}10^{-6}$ to $4.41\text{x}10^{-4}$ Kα per proton [31-33], which is much lower than the other effects, therefore we did not include ion contributions.

Conversion efficiency and temperature scaling by laser intensity

We determined the laser-electron conversion efficiency to be in the range 12–14 % at $2\text{x}10^{18}$ W cm^{-2} intensity in the 20 ps pulse with a Maxwellian temperature of 270 keV ($\overline{E} \approx 400$ keV), to 17–20 % at ~$1\text{x}10^{19}$ W cm^{-2} intensity in the 5 ps pulse with $\overline{E} \approx$ 930 keV, to 44–51 % at $3\text{x}10^{20}$ W cm^{-2} intensity regime. It is important to note that although we are unable to positively estimate the temperature at high intensity shots, we can determine the conversion efficiency by these methods. Figure 5 and 6 summarizes the temperature and the conversion efficiencies assuming Maxwellian temperatures within the entire experimental series on the Petawatt as a function of laser intensity. Deviation of the conversion efficiency results given different

temperature distributions is investigated. At a given temperature of $\overline{E}$ = 700 keV, the relativistic Maxwellian gives lowest yields among the distributions in the relevant region in these experiments. The Boltzmann gives the highest yields, so the real efficiency would be bracketed between these values (fig. 2 upper graph). Therefore using a mean electron energy is an effective characterization under these laser intensity levels.

Figure 5 shows hot electron temperature (Maxwellian) as a function of laser intensity. The temperature error bars for the 0.5 ps results in the fig. 5 represent an uncertainty determined from empirical and theoretical expectations. A scaling relation of the hot electron temperature with the laser intensity level of up to $3x10^{20}$ W cm^{-2} is determined to be $\propto I^{0.4\pm0.15}$ (1 $\propto$uncertainty) by the weighted fits.

Figure 6 shows the conversion efficiency from laser energy into the energy carried by hot electrons as a function of laser intensity. Since conversion efficiency does not have sensitivity with respect to temperature, the error bars on conversion efficiency were smaller than the temperature error bars on the figure.

Contemporaneous hard x-ray measurements show that there is 40 to 50 % of the laser energy is converted into hot electrons [11, 12]. These conversion efficiency results are consistent with the results from our K-shell measurements.

6. References

1. M. Tabak, J. Hammer, M.E. Glinsky, W.L. Kruer, S.C. Wilks, J. Woodwoth, E.M. Campbell, and M.D. Perry, "Ignition and high gain ultrapowerful lasers," Phys. Plasmas **1** p.1626 (1994.)
2. S.P. Hatchett, et. al., "Electron, photon, and ion beams from the relativistic interaction of Petawatt laser pulse with solid targets," Bull. Am. Phys. Soc. **44** p. 92 FI2.04 (1999); S.P. Hatchett, C.G. Brown, T.E. Cowan, E.A. Henry, J. Johnson, M.H. Key, J.A. Koch, A.B. Langdon, B.F. Lasinski, R.W. Lee, A.J. Mackinnon, D.M. Pennington, M.D. Perry, T.W. Phillips, M. Roth, T.C. Sangster, M.S. Singh, R.A. Snnavely, M.A. Stoyer, S.C. Wilks, and K. Yasuike, "Electron, photon, and ion beams from the relativistic interaction of Petawatt laser pulse with solid targets," Phys. Plasmas, **7** p. 2076 (2000.)
3. R.A. Snavely, M.H. Key, S.P. Hatchett, T.E. Cowan, M. Roth, T.E. Phillips, M.A. Stoyer, E.A. Henry, T.C. Sangster, M.S. Singh, S.C. Wilks, A. MacKinnon, A. Offenberger, D.M. Pennington, K. Yasuike, A.B. Langdon, B.F. Lasinski, J. Johnson, M.D. Perry, and E.M. Campbell, "Intense High Energy Proton Beams from Petawatt Laser Irradiation of Solids," Phys. Rev. Lett., to be printed (2000.) S.C. Wilks, T.E. Cowan, M. Roth, R.A. Snavely, M. Singh, S. Hatchett, M.H. Key, A.B. Langdon, D. Pennington, and A. MacKinnon, "Energetic Proton Generation in Ultra-Intense Laser-solid Interactions," Phys. Rev. Lett., in printing (2000.)
4. M. Roth, T.E. Cowan, M.H. Key, S.P. Hatchett, C. Brown, D.M. Pennington, M.D. Perry, R.A. Snavely, S.C. Wilks, and K. Yasuike, "Fast ignition by intense laser-accelerated proton beams," Phys. Lett., to be submitted.
   A.P. Fews, P.A. Norreys, F.N. Beg, A.R. Bell, A.E. Dangor, C.N. Danson, P. Lee, and S.J. Rose, "Plasma Ion Emission from High Intensity Picosecond Laser Pulse Interactions with Solid Targets," Phys. Rev. Lett. **73**, 1801 (1994.)
5. T.A. Hall, S. Ellwi, D. Batani, A. Bernardinello, V. Masella, M. Koenig, A. Benuzzi, J. Krishnan, F. Pisani, A. Djaoui, P. Norreys, D. Neely, S. Rose, M.H. Key, and P. Fews, "Fast Electron Deposition in Laser Shock Compressed Plastic Target," Phys. Rev. Lett. **81** 1003 (1998.); Paul Lee Choon Keat, "Picosecond laser-solid target interactions at Intensities Greater than 10^{18} W cm^{-2}," Ph. D. Thesis, Imperial College, University of London (1996.)
6. F.N. Beg, A.R. Bell, A.E. Dangor, C.N. Danson, A.P. Fews, M.E. Glinsky, B.A. Hammel, P. Lee, P.A. Norreys, and M. Tatarakis, "A study of picosecond laser-solid interactions up to 10^{19} W cm^{-2}," Phys. Plasmas **4** 447 (1997.)

7. M.H. Key, M.D. Cable, T.E. Cowan, K.G. Estabrook, B.A. Hammel, S.P. Hatchett, E.A. Henry, D.E. Hinkel, J.D. Kilkenny, J.A. Koch, W.L. Kruer, A.B. Langdon, B.F. Lasinski, R.W. Lee, B.J. MacGowan, A. MacKinnon, J.D. Moody, M.J. Moran, A.A. Offenberger, D.M. Pennington M.D. Perry, T.J. Phillips, T.C. Sangster, M.S. Singh, M.A. Stoyer, M. Tabak, G.L. Tietbhol, M. Tsukamoto, K. Wharton, and S.C. Wilks, "Hot electron production and heating by hot electrons in fast ignitor research," Phys. Plasmas, **5** 1966 (1998.)
K.B. Wharton, S.P. Hatchett, S.C. Wilks, M.H. Key, J.D. Moody, V. Yanovsky, A.A. Offenberger, B.A. Hammel, M.D. Perry, and C. Joshi, Phys. Rev. Lett. **81** 822 (1998.); K.B. Wharton, Ph. D. Thesis, University of California, Los Angeles (1998.)
8. M.H. Key, E.M. Campbell, T.E. Cowan, B.A. Hammel, S.P. Hatchett, E.A. Henry, J.D. Kilkenny, J.A. Koch, A.B. Langdon, B.F. Lasinski, R.W. Lee, J.D. Moody, M.J. Moran, A.A. Offenberger, D.M. Pennington, M.D. Perry, T.J. Phillips, T.C. Sangster, M.S. Singh, M.A. Stoyer, M. Tabak, M. Tsukamoto, K.B. Wharton, and S.C. Wilks, "Progress in Fast Ignitor Research with the Nova Petawatt Laser Facility," UCRL-JI-132178 Lawrence Livermore National Laboratory (November 1998.); M.H. Key et. al, "Progress in Fast Ignitor Research with the Nova Petawatt Laser Facility," Procs. of IAEA Fusion Energy 17th Conf., **IF/5** vol. 3, 1093 (1998.)
9. M.H. Key, E.M. Campbell, T.E. Cowan, S.P. Hatchett, E.A. Henry, J.A. Koch, A.B. Langdon, B.F. Lasinski, R.W. Lee, A. MacKinnon, A.A. Offenberger, D.M. Pennington, M.D. Perry, T.J. Phillips, M. Roth, T.C. Sangster, M.S. Singh, R. Snavely, M.A. Stoyer, S.C. Wilks, K. Yasuike, "Studies of the Relativistic Electron Source and Related Phenomena in Petawatt Laser Matter Interactions," (UCRL-JC-135477REV1) First Int'l Conf. On Inertial Fusion Sciences and Applications (IFSA), Bordeaux, France, Sept. 12-17, (1999.)
J.D. Hares, J.D. Kilkenny, M.H. Key, and J.G. Lunney, "Measurement of Fast-Electron Energy Spectra and Preheating in Laser-Irradiated Targets," Phys. Rev. Lett. **42** 1216 (1979.)
10. N.A. Ebrahim, C. Joshi, H.A. Baldis, "Energy deposition by hot electrons in CO2-laser-irradiated targets," Phys. Rev. **A 25**, 2440 (1982.)
11. B. Luther-Davies, A. Perry, and K.A. Nugent, "Kα emission measurements and superthermal electron transport in layered laser-irradiated disk targets," Phys. Rev. **A 35**, 4306 (1987.)

12. H. Chen, B. Soom, B. Yaakobi, S. Uchida, and D.D. Meyerhofer, "Hot-Electron Characterization from Kα Measurements in High-Contrast, p-Polarized, Picosecond Laser-Plasma Interactions," Phys. Rev. Lett **70**, 3431 (1993.)
13. A. Rousse, P. Audebert, J.P. Geindre, F. Falliès, and J.C. Gauthier, "Efficient Kα x-ray source from femtosecond laser-produced plasmas," Phys. Rev. **E 50**, 2200 (1994.)
14. Z. Jiang, J.C. Kieffer, J.P. Matte, and M. Chaker, "X-ray spectroscopy of hot solid density plasmas produced by subpicosecond high contrast laser pluses at 10^{18} – 10^{19} W/cm^2," Phys. Plasmas **2**, 1702 (1995.)
15. U. Teubner, I. Uschmann, P. Gibbon, D. Altenbernd, E. Förster, T. Feurer, W. Theobald, R. Sauerbrey, G. Hirst, M.H. Key, J. Lister, and D. Neely, "Absorption and hot electron production by high intensity femtosecond UV-laser pluses in solid targets," Phys. Rev. **E 54** 4167 (1996.)
16. Private communications with K.A. Tanaka at ILE, Osaka University, Japan.
17. Th. Schlegel, S. Bastiani, L. Grémillet, J. -P. Geindre, P. Audebert, J.-C. Gauthier, E. Lefebvre, G. Bonnaud, and J. Delettrez, "Comparison of measured and calculated x-ray and hot-electron production in short-pulse laser-solid interactions at moderate intensities," Phys. Rev. **E 60**, 2209 (1999.)
18. S. Bastiani, P. Audebert, J.P. Geindre, Th. Schlegel, and J.C. Gauthier, "Hot-electron distribution functions in a subpicosecond laser interaction with solid targets of varying initial gradient scale lengths," Phys. Rev. **E 60** 3439 (1999.)
19. M.D. Perry, D. Pennington, B.C. Stuart, G. Tietbohl, J.A. Britten, C. Brown, S. Herman, B. Golick, M. Kartz, J. Miller, H.T. Powell, M. Vergino, and V. Yanovsky, "Petawatt laser pluses," Optics Lett. **24** 160 (1999.)
20. Scott C. Wilks, and William L. Kruer, "Absorption of Ultrashort, Ultra-Intense Laser Light by Solids and Overdense Plasmas," IEEE J. of Quantum Electronics IEJQA7 **33**, 1954 (1997.); W.L. Kruer, and S.C. Wilks, "Introduction to ultra-intense laser-plasma interactions," in "Advances in Plasma Physics," AIP, New York, p. 16-25, (1994.)
21. D.E. Cullen, et. al, "Tables and Graphs of Photon-Interaction Cross Sections from 10 eV to 100 GeV Derived from the LLNL Evaluated Photon Data Library (EPDL,) Part A: Z=1 to 50, Part B: Z=51 to 100," UCRL-50400, **6** Rev. 4, Lawrence Livermore National Laboratory (October 1989.); D.E. Cullen, et. al, "The 1989 Livermore Evaluated Photon Data Library (EPDL,)" UCRL-ID-103424, Lawrence Livermore National Laboratory (March 1990.); S.T. Perkins, et. al, "Tables and Graphs of Atomic Subshell and Relaxation Data Derived from

the LLNL Evaluated Atomic Data Library (EADL)," UCRL-50400, **30**, Lawrence Livermore National Laboratory (October 1991.)

22. G. Audi, and A.H. Wapstra, "The 1995 update to the atomic mass evaluation," Nuclear Physics **A595** 409-480 (1995.); S.Y.F. Chu, L.P. Ekstr, and R.B. Firestone, "WWW Table of Radioactive isotopes, database version 2/28/99 from URL http://nucleardata.nuclear.lu.se/nucleardata/toi/" (1999.)
23. J.A. Halbleib, and T.A. Mehlhorn, Nucl. Sci. Eng. **92**, 338 (1986.); "ITS Version 3.0: The Integrated TIGER Series of Coupled Electron/Photon Monte Carlo Transport Codes," SAND91-1634 (March 1992.)
24. SITe Lit. No. SI-003A, version date: 12/21/95, http://www.site-inc.com/pdf/003datsh.pdf.
25. D.H. Lumb, E.G. Chowanietz, and A. Wells, "X-ray measurements of charge diffusion effects in EEV Ltd. Charge-coupled devices." Optical Engineering, **26** 773 (1987.); D.H. Lumb, and A.D. Holland, "Event Recognition Techniques in CCD X-ray Detectors for Astronomy," Nuclear Inst. and Method D.H. Lumb, and A.D. Holland, Nuclear Inst. and Method V. High Energy Astrophysics p. 696 (1988.)
26. K. Yasuike, et. al, "Diagnostic of hot electron in a solid laser target from ultra-intense laser-plasma interaction ($3x10^{20}$ W cm^{-2}, $\leq$ 400 J) by K-shell lines measurements," Rev. of Sci. Inst. (submitted) (2000.)
27. Md Rashiduzzaman Khan, D. Crumpton, and P.E. Francois, "Proton induced x-ray production in titanium, nickel, copper, molybdenum and silver," J. Phys. B **9** p. 455 (1976.)
28. T.K. Li, and R.L. Watson, "Kβ/Kα intensity ratio for x-ray production by fast deuterons, particles, and carbon ions," Phys. Rev. **A9** p. 1574 (1974.)
29. J.D. Garcia, R.J. Fortner, and T.M. Kavanagh, "Inner-Shell Vacancy Production in Ion-Atom Collisions," Rev. of Modern Phys. **45** 111 (1973.)

Figure captions

Fig. 1

Experimental set-up. Laser was focused by the on-axis f/3 parabolic mirror onto the target. In-set 1 shows the target structure. Front layer thickness used in these experiments were from 200 μm to 1000 μm. In-set 2 shows the reflex electrons, which possibly produce K-shell x-rays at the tracer layer and cause errors. The protective layer reduces K-shell signal by those electrons by factor 2.

Fig. 2

Universal curves, Kα production yields from 50 μm Mo layer as a function of Boltzmann (in blue), Maxwellian (in green) or relativistic Maxwellian (in red) temperature are shown (left and bottom axis). Each temperature distribution set has four curves for the different front layer thicknesses used in these experiments: 200 μm, 400 μm, 800 μm and 1000 μm Al. The universal curves are calculated for the observation angle of within 30–45° cone angle normal to the target (and laser) axis. Upper graphs (right axis) shows a ratio of Boltzmann (relativistic Maxwellian) Kα yields to

Maxwellian at same average energy $\overline{E}$,by which Boltzmann, Maxwellian, and relativistic Maxwellian temperature described as $\overline{E}$, $2\overline{E}/3$, and $\overline{E}/3$, respectively.

Fig. 3

K-shell photon production yields results for 20 ps (a), 5 ps (b) and 0.5 ps (c) are shown. Curves in blue, green and red represent Boltzmann, Maxwellian and relativistic-Maxwellian temperatures for the fits. In (a) and (b): All the points are Kα results. Solid curves show weighted chi-square fit results to estimate the conversion efficiencies and the temperatures and dashed curves for unweighted fits to estimate uniform errors ($\sigma_{\text{uniform-}\chi 2}$'s) from chi-squares; The thick error bars in extremely right in light blue show the uniform chi-squares form the fits. In (c): Kβ results (the points in red) are plotted against the right axis, which scaled 0.18123 to the left Kα axis (the points in blue) to directly compare the Kα and Kβ results; Uniform errors for the 0.5 ps shots are calculated using Kβ results only ($\sigma_{\chi 2\,K\beta}$'s), shown in extremely right, and using both Kα and Kβ results ($\sigma_{\chi 2\,K\alpha\&\beta}$'s),, in extremely left; dotted curves in above show 100 % yields curves for a mean electron energy of 2 MeV.

Fig. 4

Chi-square behavior for 20 ps (circle points), 5 ps (triangles) and 0.5 ps (squares) data sets as a function of presumed Maxwellian temperature are shown in bottom graph. Top graph shows the conversion efficiency behavior at the same time. The temperature for 20 ps data can be estimated positively from the chi-square convergence (dip), and in same time, convergence efficiencies are not very sensitive in either case. As laser intensity increases, sensitivity to determination of temperature by chi-square behavior decreases.

Fig. 5

Hot electron temperature (Maxwellian) as a function of laser intensity are shown. The temperature error bars for the 0.5 ps results represent uncertainty determined from empirical and theoretical expectations. Scaling relation of the hot electron temperature under the laser intensity level of up to $3x10^{20}$ W cm^{-2} is determined to be $\propto I^{0.4\pm0.15}$ by the fits weighted using the error bars.

Fig. 6

Conversion efficiency from laser energy into the energy carried by hot electrons as a function of laser intensity is plotted. Since conversion efficiency does not have sensitivity against the temperature, the error bars on conversion efficiency were smaller than the temperature error bars on the fig. 5.

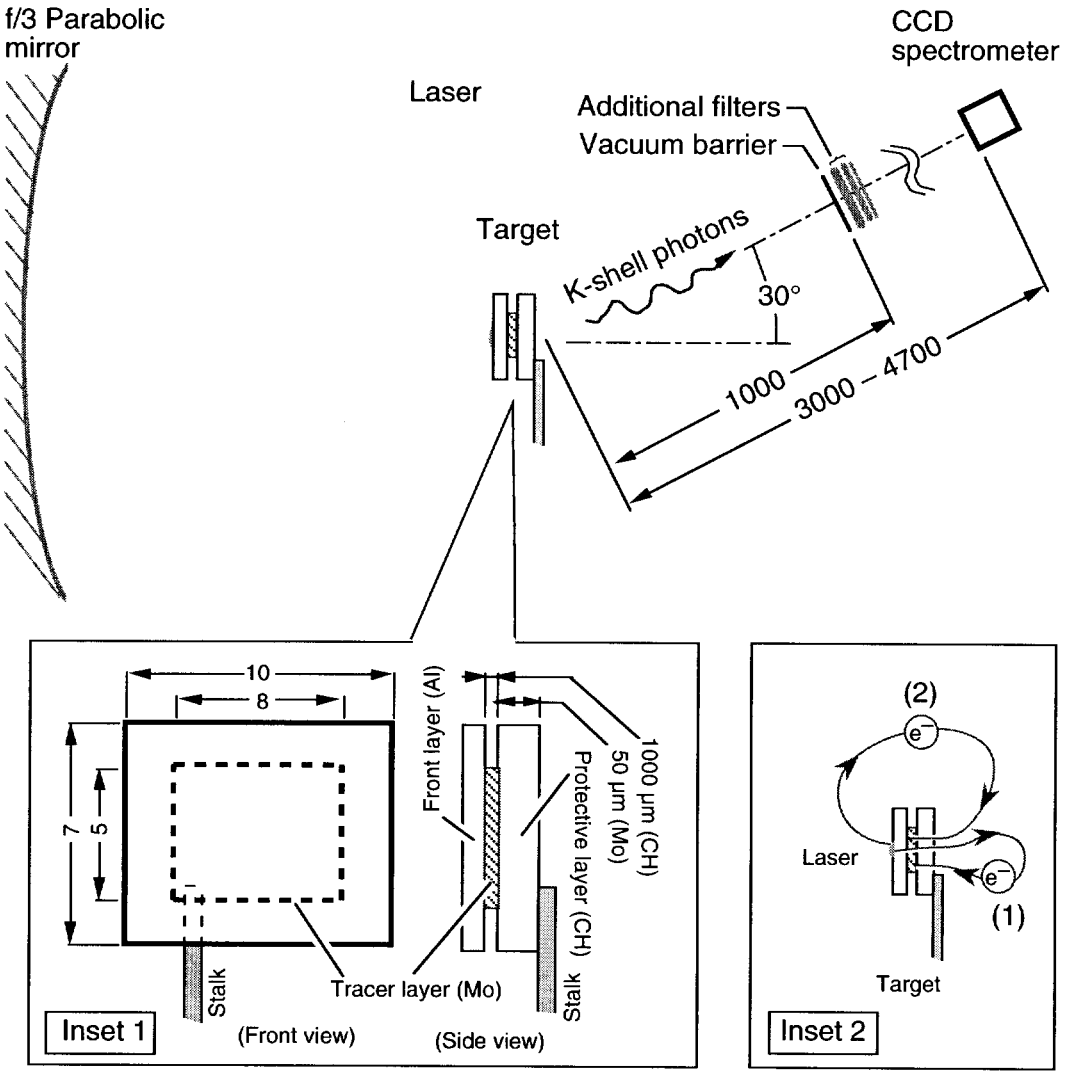

Notes: Dimensions in mm otherwise noted (1 mm = 39.37 mil); Not to scale.

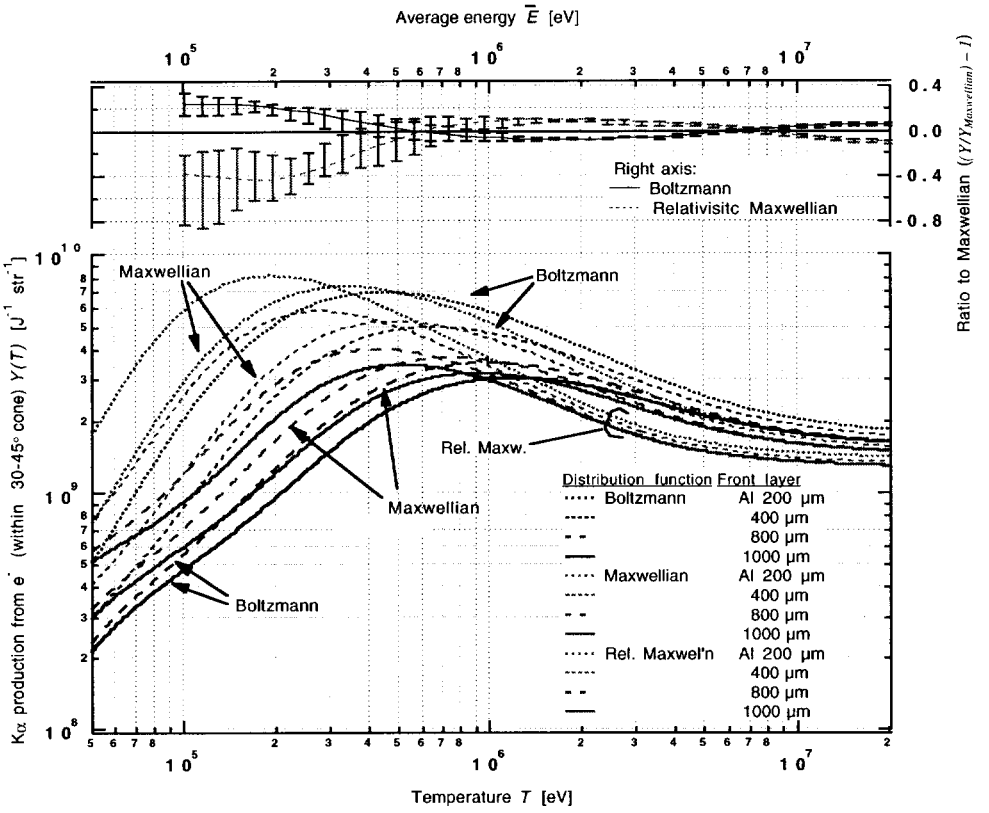
Average energy $\bar{E}$ [eV]
Right axis:
Boltzmann
Relativisitc Maxwellian
Ratio to Maxwellian $((Y/Y_{Maxwellian}) - 1)$
Maxwellian
Boltzmann
Rel. Maxw.
Maxwellian
Boltzmann
Distribution function Front layer
Boltzmann Al 200 μm
400 μm
800 μm
1000 μm
Maxwellian Al 200 μm
400 μm
800 μm
1000 μm
Rel. Maxwel'n Al 200 μm
400 μm
800 μm
1000 μm
Kα production from e⁻ (within 30-45° cone) Y(T) [J⁻¹ str⁻¹]
Temperature T [eV]

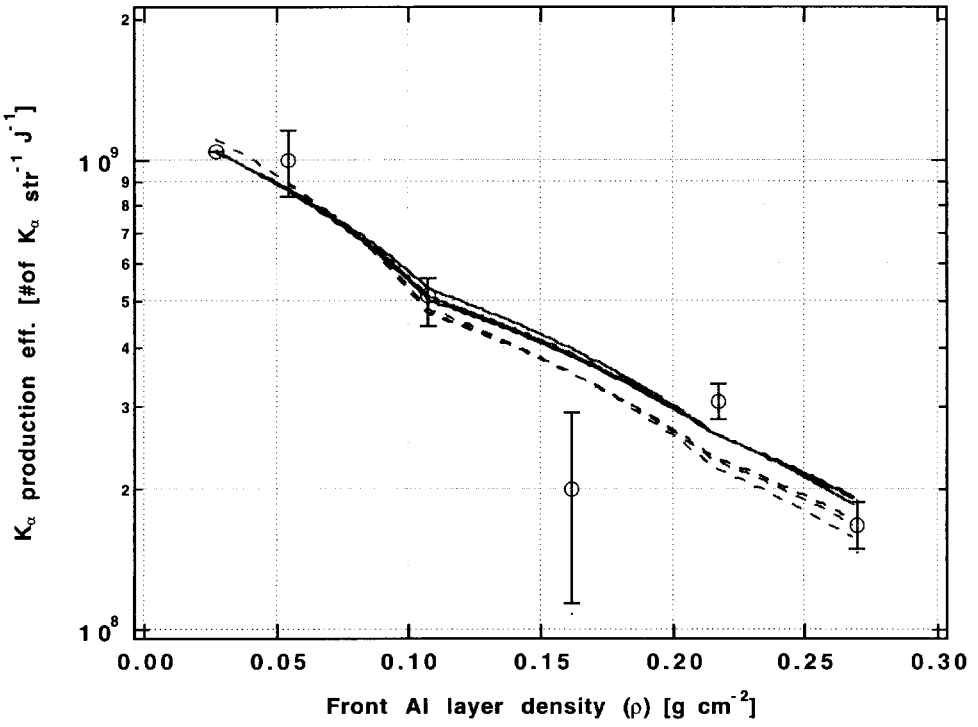
Kα production eff. [#of Kα str⁻¹ J⁻¹]
Front Al layer density (ρ) [g cm⁻²]

(b)

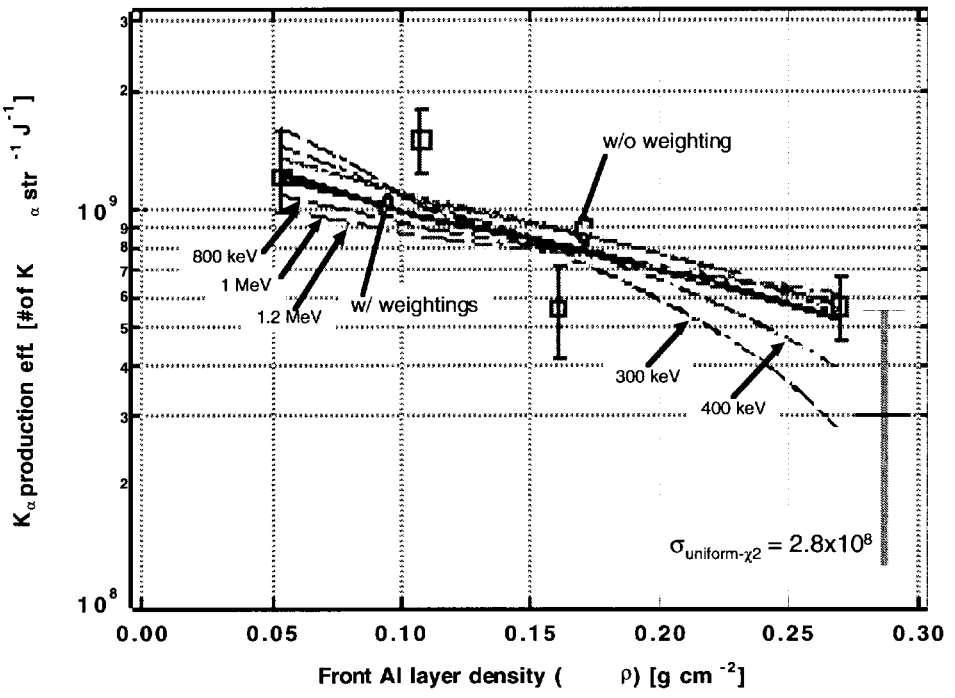

Fig. 3-b The 5 ps experimental results.

4

(c)

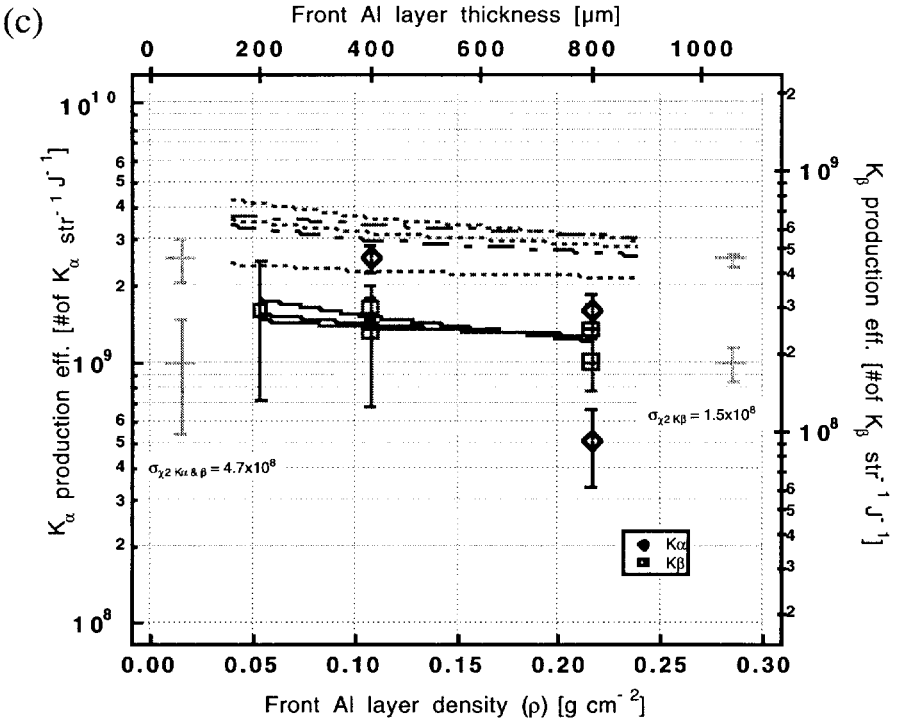

Fig. 3-c The 0.5 ps experimental results.

5

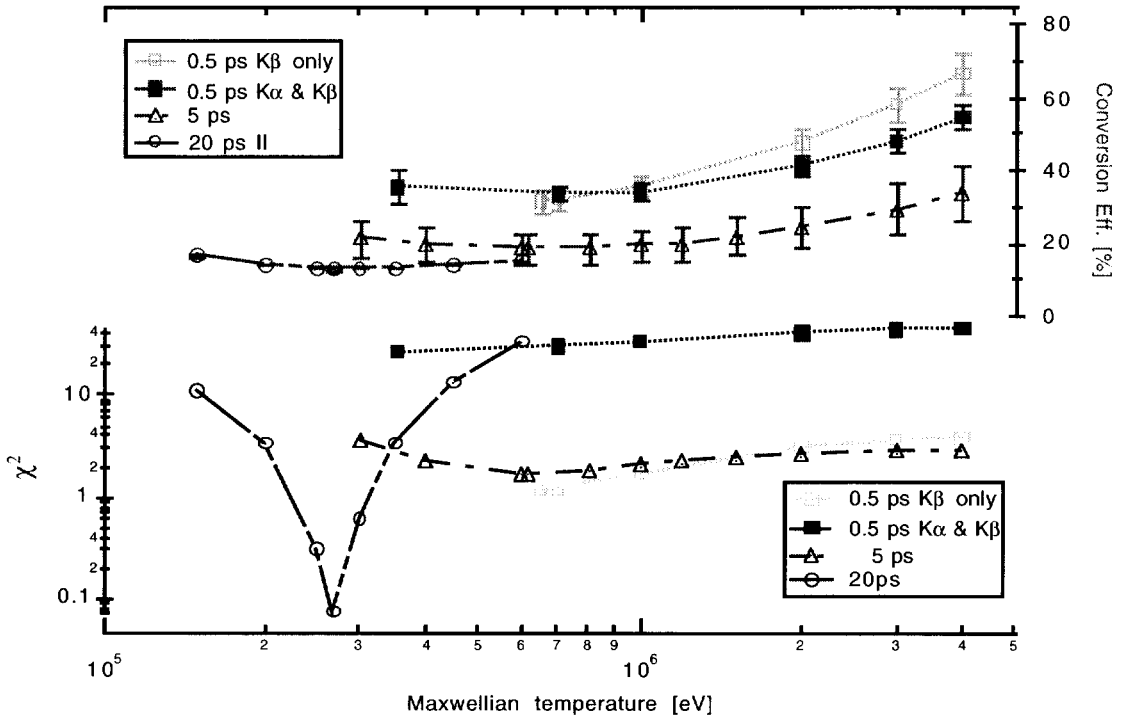

Fig. 4 Conversion eff. and χ^2 vs. presumed Maxw. temp.

6

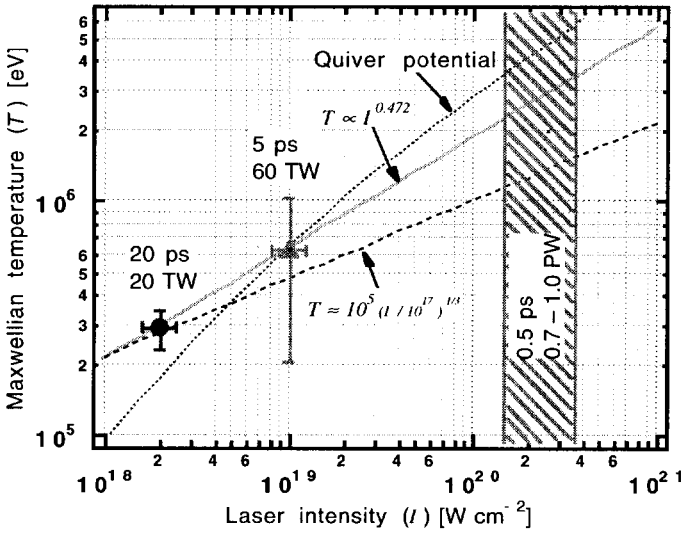

Fig. 5 Hot electron temperature overview

7

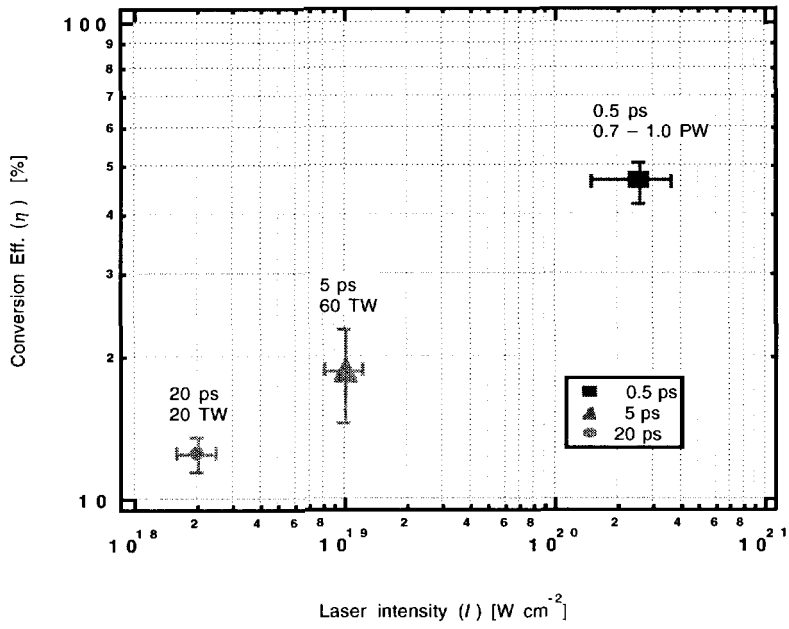

Fig. 6 Hot electron conversion efficiency scaling